Journal of the Brazilian Society of Mechanical Sciences and Engineering (2022) 44:227
https://doi.org/10.1007/s40430-022-03451-9

TECHNICAL PAPER

Further analysis of double-diffusive flow of nanofluid through a porous medium situated on an inclined plane: AI-based Levenberg–Marquardt scheme with backpropagated neural network

Muhammad Shoaib[1] · Tabassum Rafia[1] · Muhammad Asif Zahoor Raja[2] · Waqar Azeem Khan[3,4] · Muhammad Waqas[5]

Received: 11 June 2021 / Accepted: 24 February 2022 / Published online: 10 May 2022
© The Author(s), under exclusive licence to The Brazilian Society of Mechanical Sciences and Engineering 2022

Abstract
The present article exploits a novel application of AI-based Levenberg–Marquardt scheme with backpropagated neural network (LMS–BPNN) to analyze the double-diffusive free convection nanofluid flow model (DDFC-NFM) over an inclined plate in the existence of Brownian motion and thermophoresis properties embedded in a porous medium. The governing PDEs representing DDFC-NFM are transformed into system of nonlinear ODEs by applying suitable transformation. The reference data set is generated from Lobatto III-A numerical solver by variation of magnetic field parameter (M), thermal Grashof number (Gr), angle of inclination (α), Brownian motion parameter (Nb), Dufour-solutal Lewis number (Ld), modified Dufour parameter (Nd) and thermophoresis parameter (Nt) for all scenarios of the designed LMS–BPNN. The approximate solution and its comparison with standard solution are analyzed by execution of training, testing and validation procedure of the designed LMS–BPNN. The effectiveness and reliable performance of LMS–BPNN are endorsed with MSE-based fitness curve, regression analysis, error histogram analysis and correlation index. Results reveal that velocity increases with the rise in *Gr,* whereas reverse trend has been noticed for angle of inclination and magnetic field parameter and the temperature profile increases with the increase in Nb, Nd and Nt. The solutal concentration profile increases with the increment in Ld, while an increase in Nd causes a decrease in it. When Nt increases, the enhancement in the nanoparticle volume frictions occurs, but an opposite behavior is depicted for Brownian motion parameter.

Keywords Double-diffusive free convection · Nanofluid · Thermophoresis and Brownian motion effect · numerical computation · Artificial backpropagated neural network · Levenberg–Marquardt scheme

List of symbols

u, v	Velocity components
B_0	Magnetic field strength
y μ	Dynamic viscosity
ρ_f	Base fluid density
σ	Electrical conductivity
D_{B}	Brownian motion coefficient
T	Temperature
T_∞	Ambient temperature
N_∞	Ambient volume friction
K'	Porous medium permeability

Technical Editor: Ahmad Arabkoohsar.

This article has been selected for a Topical Issue of this journal on Nanoparticles and Passive-Enhancement Methods in Energy.

✉ Waqar Azeem Khan
waqarazeem@bit.edu.cn; waqar_qau85@yahoo.com

[1] Department of Mathematics, COMSATS University Islamabad, Attock Campus, Attock 43600, Pakistan

[2] Future Technology Research Center, National Yunlin University of Science and Technology, 123 University Road, Section. 3, Douliou 64002, Yunlin, Taiwan, ROC

[3] Nonlinear Analysis and Applied Mathematics (NAAM) Research Group, Department of Mathematics, Faculty of Science, King Abdulaziz University, Jeddah, Saudi Arabia

[4] Department of Mathematics, Mohi-ud-Din Islamic University, Nerian Sharif, Azad Jammu and Kashmir 12010, Pakistan

[5] NUTECH School of Applied Sciences and Humanities, National University of Technology, Islamabad 44000, Pakistan

D_{TC}	Dufour-kind diffusivity
Gr	Thermal Grashof number
Gm	Solutal Grashof number
Nb	Brownian motion parameter
M	Magnetic field parameter
Ln	Nanoliquid Lewis number
Ld	Dufour-solutal Lewis number
Nt	Thermophoresis parameter
DDFC	Double-diffusive free convection
NFM	Nanofluid flow model
Pr	Prandtl number
v	Kinematic viscosity
g	Gravitational force
ρ_p	Nanoparticle mass density
τ	Ratio of heat capacities
α_1	Thermal diffusivity
D_T	Thermophoretic diffusion coeff.
C_∞	Ambient concentration
D_S	Solutal diffusivity
D_{CT}	Dufour-kind diffusivity
α	Angle of inclination
G_n	Nanoparticle Grashof number
Nd	Modified Dufour parameter
MSE	Mean square error
Le	Regular Lewis number
K	Permeability parameter
γ	Nanoparticle volume fraction
ANN	Artificial neural network
LMS	Levenberg–Marquardt scheme
BPNN	Backpropagated neural network

1 Introduction

In recent time, nanofluid and its findings have received significance importance over the past few years. This is due to their diverse and massive applications such as nano-drug delivery, food processing, power plant, geothermal extraction, nanoliquid detergent and numerous others. Firstly, the word 'nanofluid' was invented by Choi [1] which is a liquid composed of nano-scaled particle suspended in base fluid. This nanometer-sized material has unique chemical and physical characteristics. Usually, the base fluid has low thermal conductivity such as water, engine oil and ethylene glycol used for this purpose, and the nanoparticles consist of Cu, AlN, SiC, Al_2O_3 and graphite. It supports base fluid as due to high thermal conductivity it enhances the heat transfer process which saves cost and times. Several authors investigated nanofluid flow past an inclined plate under different effects. Khan et al. [2] studied viscosity of MHD flow of mixed convection Eyring–Powell nanofluid past an inclined plate. Zeeshan et al. [3] numerically investigated bi-phase coupled stress nanofluid past an inclined surface with Hafnium and metallic nanoparticles. Laminar conjugate mixed convection flow of nanofluid with transverse magnetic field past an inclined flat surface embedded in a porous medium is discussed by Khademi et al. [4]. Mass and energy transport boundary-layer flow of nanofluid in the presence of Soret–Dufour effect past an inclined plate is presented by Rafique et al. [5]. Idowu and Falodun [6] analyzed the heat and mass transfer MHD flow of nanofluid past an inclined surface in the existence of thermophoresis and Soret–Dufour effect. Recently, the researchers also investigated the combination of three different nanoparticles with base liquid, known as ternary hybrid fluid. The viscosity and thermal conductivity of these fluids depend upon three volume fraction parameters. Animasaun et al. [7] exemplified the three-dimensional ternary nanofluids considering suction effect and bi-stretching surface. Yook et al. [8] investigated the ternary fluid past convectively heated sheet considering the effect of heat sink/source and magnetic flux density.

Many authors investigated the non-Newtonian fluid and its findings over a porous medium [9–11]. Rashad et al. [12] exemplified natural convective non-Newtonian nanofluid flow in a porous medium past a radiative plate. Slip motion of MHD nanofluid over a stretching surface in porous media is examined by Kumar et al. [13]. Megahed [14] studied within a porous medium the convective heat transfer effect past a Maxwell fluid flow past a stretching surface. Rasheed et al. [15] discussed mixed convection flow of tangent hyperbolic fluid implanted in a porous medium with chemically reactive and magnetic field effect. Heat transfer effect on peristaltic propulsion of Jeffrey nanofluid within a porous rectangular medium is presented by Riaz et al. [16]. Yadav [17] analyzed the effect of Darcy number and viscosity on the arrival of convective motion in a couple-stress fluid in a porous medium.

The effect of concentration with temperature gradient referring to buoyancy-driven flows is known as double-diffusive convection. The double-diffusive convention has a variety of applications in scientific field such as oceanography, geophysics applications, chemical reaction, petroleum reservoirs, aerospace defense, solar collector, food processing, energy storage and numerous others. Firstly, Pera and Gebhart [18] investigated numerically this phenomenon for vertical laminar fluid motions. After this, numerous studies have been investigated on double diffusion [19–21]. Nag and Molla [22] studied the double-diffusive natural convention effect on non-Newtonian nanofluid in square cavity. Double-diffusion effect over square cavity on natural convention flow with entropy generation is investigated by Said et al. [23]. The suspension of nano-encapsulated phase change materials in the presence of double-diffusion nanofluid flow in rotating porous cavity is examined by Raizah and Aly [24]. Prasad et al. [25] analyzed the double-diffusion natural convection Casson nanoliquid flow over an inclined surface within a Darcian porous medium. MHD Casson fluid past a vertically inclined plane in a porous medium with double-D = diffusion convective flow is discussed by Sailaja et al. [26]. Double-diffusion effect on mixed convection flow in the existence of static magnetic field within rectangular domain is investigated by Moolya and Satheesh [27].

The natural convective boundary-layer nanofluid flow in the presence of Brownian and thermophoresis effect is taking into consideration by many researchers [28, 29]. The suspension of randomly moving particles in gas or liquid which enhance the collision of molecules is known as Brownian motion, whereas thermophoresis is the movement of tiny particles toward decreasing thermal gradient. Heat transfer free convection nanofluid flow with Brownian and thermophoresis effect is studied by Haddad et al. [30]. Ganji et al. [31] examined the Brownian and thermophoresis effect on free convection MHD Al_2O_3–H_2O nanofluid flow. Heat transfer natural convection flow on nanofluid with Brownian and thermophoresis effect in *L*-shaped enclosure is studied by Rana et al. [32]. The effect of Brownian motion and thermophoresis in wavy porous cavity on free convection nanofluid flow is presented by Pop et al. [33].

Sometimes, it is not possible to find an exact solution of a problem analytically for this purpose; researcher uses different numerical and semi-numerical techniques to solve the problem. Some techniques are homotopy perturbation method [34], Keller–Box method [35], spectral relaxation method [36], Galerkin finite element method [21] and many others [37–39]. All the above-mentioned cited studies on different nanofluidic systems are solved by using different numerical and semi-numerical methods, but AI-based numerical computing paradigms are important to exploit double-diffusive free convection nanofluid flow model (DDFC-NFM) due to their worthiness and efficiency. Some authors already applied these stochastic numerical techniques in different fields such as thermodynamic [40], plasma physics [41], astrophysics [42], finance [43], nanofluid model [44], Emden–Fowler system [45, 46], HIV infection model [47], nonlinear corneal shape model [48], mosquito dispersal model [49] and COVID-19 models [50, 51]. All these inspiring factors motivate the researchers to exploit consistent and precise AI algorithm-based numerical computational paradigm for numerical analysis of mathematical model for double-diffusive free convection nanofluid by conducting graphical and numerical studies to explore the effect of all variants on velocity, nanoparticle volume fraction, solutal concentration and temperature profile. MATLAB is used for this purpose.

The innovative contributions of the present study are as follows:

- The novel application of Levenberg–Marquardt scheme with backpropagated neural network (LMS–BPNN) is adopted to analyze the double-diffusive free convection nanofluid flow model (DDFC-NFM) over an inclined plane in the existence of thermophoresis and Brownian motion properties implanted within a porous medium.
- The mathematical modeling is presenting for the proposed problem, i.e., DDFC-NFM.
- The reference data set is generated from Lobatto III-A numerical solver by the variation of and for all seven scenarios of the designed LMS–BPNN.
- The solver LMS–BPNN is designed with the help of procedure based on testing, training and validation to find the approximate solutions of DDFC-NFM. Furthermore, the comparative study is conducted through MSE in order to validate the consistent accuracy.
- The effectiveness and reliable performance of LMS–BPNN are endorsed with MSE-based fitness curve, regression analysis, error histogram analysis and correlation index.

2 Problem formulation

Consider time-independent 2D incompressible natural convection flow of nanofluid past an inclined impermeable plate implanted in the existence of thermophoresis and Brownian motion effect within a porous medium. Figure 1 represents the geometry of the present fluid flow system, where y-axis is perpendicular to an inclined plate and x-axis makes an acute angle α with vertical part.

A uniform transverse magnetic field of strength B_0 is applied normal toward the direction of nanofluid flow. The

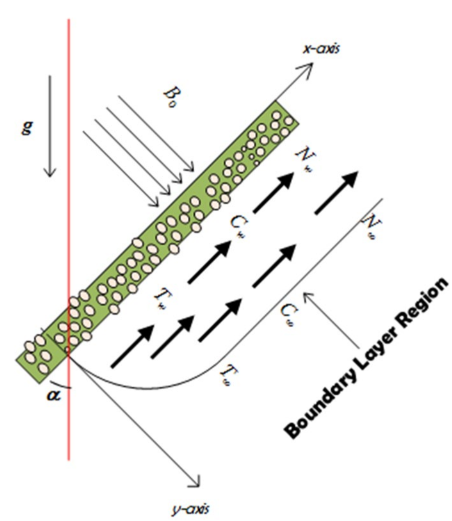

Fig. 1 Flow model

influence of induced magnetic field and magnetic Reynolds number is negligible. Further, we consider the temperature T_w, the solute concentration C_w and nanoparticle volume fraction N_w have constant values. Ambient values of T, C and N are T_∞, C_∞ and N_∞, respectively. Assume $C_w > C_\infty$ and $N_w < N_\infty$, so that as a consequence thermal and nanoparticle volume fraction buoyancy effect of an upward fluid is encouraged.

The system of PDEs with BCs after considering Soret and Dufour effect is as follows [52–54]:

$$\frac{\partial u}{\partial x}+\frac{\partial v}{\partial y}=0, \tag{1}$$

$$\rho_f\left(\frac{\partial u}{\partial x}u+\frac{\partial u}{\partial y}v\right)=\left(\frac{\partial^2 u}{\partial y^2}\right)\mu-\sigma u B_0^2-\frac{u\mu}{K'} +g\cos\alpha\left(\begin{array}{l}\left((C-C_\infty)\beta^*+(T-T_\infty)\beta\right)\rho_{f\infty}(1-N_\infty)\\-(N-N_\infty)(\rho_p-\rho_{f\infty})\end{array}\right), \tag{2}$$

$$\frac{\partial T}{\partial x}u+\frac{\partial T}{\partial y}v=\frac{\partial^2 T}{\partial y^2}\alpha_1+\left(\left(\frac{\partial T}{\partial y}\right)^2\frac{D_T}{T_\infty}+\frac{\partial T}{\partial y}\frac{\partial N}{\partial y}D_{\mathrm{B}}\right)\tau + \frac{\partial^2 C}{\partial y^2}D_{\mathrm{TC}}, \tag{3}$$

$$\frac{\partial C}{\partial x}u+\frac{\partial C}{\partial y}v=\frac{\partial^2 C}{\partial y^2}D_{\mathrm{S}}+\frac{\partial^2 T}{\partial y^2}D_{\mathrm{CT}}, \tag{4}$$

$$\frac{\partial N}{\partial x}u+\frac{\partial N}{\partial y}v=\frac{\partial^2 N}{\partial y^2}D_{\mathrm{B}}+\frac{\partial^2 T}{\partial y^2}\left(\frac{D_T}{T_\infty}\right), \tag{5}$$

$$\begin{array}{ll} u=0,\ v=0,\ N=N_w,\ C=C_w,\ T=T_w, & \text{at } y=0,\\ u\to 0,\ C\to C_\infty, N\to N_\infty,\ T\to T_\infty, & \text{as } y\to\infty. \end{array} \tag{6}$$

Consider dimensionless variables [55]:

$$x'=x\left(\frac{c}{\nu}\right)^{1/2},\ y'=y\left(\frac{c}{\nu}\right)^{1/2},\ u'=\frac{u}{(c\nu)^{1/2}},\ v'=\frac{v}{(c\nu)^{1/2}}, \theta=\frac{T-T_\infty}{T_w-T_\infty},\ \gamma=\frac{N-N_\infty}{N_w-N_\infty},\ \phi=\frac{C-C_\infty}{C_w-C_\infty}, \tag{7}$$

Here, c is the empirical constant. The following equations can be attained by substituting the above variables:

$$\frac{\partial u}{\partial x}+\frac{\partial v}{\partial y}=0, \tag{8}$$

$$\frac{\partial u}{\partial x}u+\frac{\partial u}{\partial y}v=\frac{\partial^2 u}{\partial y^2}-(K+M)u-\gamma\mathrm{Gn}\cos\alpha+\phi\mathrm{Gm}\cos\alpha +\theta\mathrm{Gr}\cos\alpha=0, \tag{9}$$

$$u+\frac{\partial\theta}{\partial y}v=\frac{\partial^2\theta}{\partial y^2}\frac{1}{\mathrm{Pr}}+\left(\frac{\partial\theta}{\partial y}\right)^2\mathrm{Nt}+\frac{\partial\theta}{\partial y}\frac{\partial\gamma}{\partial y}\mathrm{Nb}+\frac{\partial^2\phi}{\partial y^2}\mathrm{Nd}=0, \tag{10}$$

$$\left(\frac{\partial\phi}{\partial x}u+\frac{\partial\phi}{\partial y}v\right)\mathrm{Le}=\frac{\partial^2\phi}{\partial y^2}+\frac{\partial^2\theta}{\partial y^2}\mathrm{Ld}, \tag{11}$$

$$\left(\frac{\partial\phi}{\partial x}u+\frac{\partial\phi}{\partial y}v\right)\mathrm{Ln}=\frac{\partial^2\phi}{\partial y^2}+\frac{\partial^2\theta}{\partial y^2}\frac{\mathrm{Nt}}{\mathrm{Nb}}, \tag{12}$$

$$\begin{array}{ll} u=0, v=0, \theta=1, \gamma=1, \phi=1, & \text{at } y=0,\\ \frac{\partial\psi}{\partial y}\to 0,\ \gamma\to 0,\ \phi\to 0,\ \theta\to 0, & \text{at } y\to\infty. \end{array} \tag{13}$$

Mathematical expressions for physical parameters used in Eqs. (8)–(12) are:

$$\mathrm{Gr}=\frac{g\rho_{f\infty}\beta(T_w-T_\infty)(1-N_\infty)}{c\rho_f(c\nu)^{1/2}},\quad \mathrm{Gm}=\frac{g\rho_{f\infty}\beta^*(C_w-C_\infty)(1-N_\infty)}{c\rho_f(c\nu)^{1/2}},$$
$$\mathrm{Gn}=\frac{g(\rho_p-\rho_{f\infty})(N_w-N_\infty)}{c\rho_f(c\nu)^{1/2}},\quad M=\frac{B_0^2\sigma}{c\rho_f},\quad K=\frac{\nu}{cK'},\quad \mathrm{Pr}=\frac{\nu}{\alpha},$$
$$\mathrm{Nt}=\frac{(T_w-T_\infty)D_T\tau}{T_\infty\nu},\quad \mathrm{Nb}=\frac{(N_w-N_\infty)D_{\mathrm{B}}\tau}{\nu},\quad \mathrm{Nd}=\frac{(C_w-C_\infty)D_{\mathrm{TC}}}{(T_w-T_\infty)\nu},$$
$$\mathrm{Le}=\frac{\nu}{D_{\mathrm{S}}},\ \mathrm{Ln}=\frac{\nu}{D_{\mathrm{B}}},\quad \mathrm{Ld}=\frac{(T_w-T_\infty)D_{\mathrm{CT}}}{(C_w-C_\infty)D_{\mathrm{S}}}.$$

Involving stream function

$$\frac{\partial\psi}{\partial y}=u,-\frac{\partial\psi}{\partial x}=v,$$

we have the following form of Eqs. (9)–(13) as:

$$\frac{\partial^2\psi}{\partial x\partial y}\frac{\partial\psi}{\partial y}-\frac{\partial^2\psi}{\partial y^2}\frac{\partial\psi}{\partial x}=\frac{\partial^3\psi}{\partial y^3}-(K+M)\frac{\partial\psi}{\partial y} -\gamma\mathrm{Gn}\cos\alpha+\phi\mathrm{Gm}\cos\alpha+\theta\mathrm{Gr}\cos\alpha=0, \tag{14}$$

$$\frac{\partial\theta}{\partial x}\frac{\partial\psi}{\partial y}-\frac{\partial\theta}{\partial y}\frac{\partial\psi}{\partial x}=\frac{\partial^2\theta}{\partial y^2}\frac{1}{\mathrm{Pr}} +\left(\frac{\partial\theta}{\partial y}\right)^2\mathrm{Nt}+\frac{\partial\theta}{\partial y}\frac{\partial\gamma}{\partial y}\mathrm{Nb}+\frac{\partial^2\phi}{\partial y^2}\mathrm{Nd}=0, \tag{15}$$

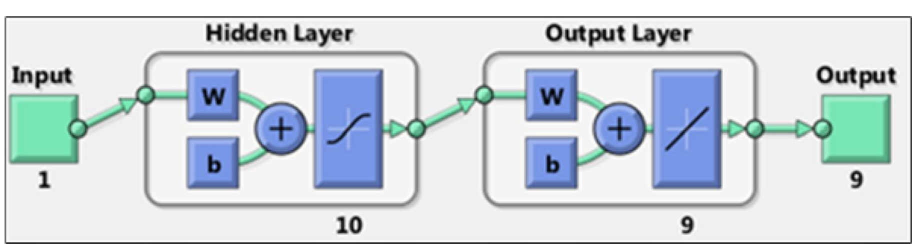

Fig. 2 The neural network for DDFC-NFM

$$\left(\frac{\partial \phi}{\partial x}\frac{\partial \psi}{\partial y}-\frac{\partial \phi}{\partial y}\frac{\partial \psi}{\partial x}\right)\mathrm{Le}=\frac{\partial^2 \phi}{\partial y^2}+\frac{\partial^2 \theta}{\partial y^2}\mathrm{Ld}, \tag{16}$$

$$\left(\frac{\partial \phi}{\partial x}\frac{\partial \psi}{\partial y}-\frac{\partial \phi}{\partial y}\frac{\partial \psi}{\partial x}\right)\mathrm{Ln}=\frac{\partial^2 \phi}{\partial y^2}+\frac{\partial^2 \theta}{\partial y^2}\frac{\mathrm{Nt}}{\mathrm{Nb}}, \tag{17}$$

$$\begin{aligned}&\tfrac{\partial \psi}{\partial x}=0, \tfrac{\partial \psi}{\partial y}=0, \theta=1, \gamma=1, \phi=1, \text{ at } y=0,\\ &\tfrac{\partial \psi}{\partial y}\rightarrow 0,\ \gamma\rightarrow 0,\ \ \phi\rightarrow 0,\ \ \theta\rightarrow 0, \text{ as } \ y\rightarrow\infty.\end{aligned} \tag{18}$$

The further information regarding problem formulation can be seen in [55]. The process of finding the solution of the above PDEs is complex and tough. Lie group transformations suggested by Mukhopadhyay et al. [56, 57] and Islam et al. [58] are applied to solve the system of PDEs.

This implies the following are corresponding ODEs with boundary conditions.

$$\begin{aligned}&\frac{\mathrm{d}^3 f}{\mathrm{d}\eta^3}+\frac{3}{4}f\frac{\mathrm{d}^2 f}{\mathrm{d}\eta^2}-\frac{1}{2}\left(\frac{\mathrm{d}f}{\mathrm{d}\eta}\right)^2-(M+K)\frac{\mathrm{d}f}{\mathrm{d}\eta}\\ &\quad-\gamma \mathrm{Gn}\cos\alpha+\phi \mathrm{Gm}\cos\alpha+\theta \mathrm{Gr}\cos\alpha=0,\end{aligned} \tag{19}$$

$$\frac{\mathrm{d}^2 \theta}{\mathrm{d}\eta^2}+\frac{3}{4}\,\mathrm{Pr} f\frac{\mathrm{d}\theta}{\mathrm{d}\eta}+\left(\frac{\mathrm{d}\theta}{\mathrm{d}\eta}\right)^2\mathrm{Nt}+\frac{\mathrm{d}\theta}{\mathrm{d}\eta}\frac{\mathrm{d}\gamma}{\mathrm{d}\eta}\mathrm{Nb}+\frac{\mathrm{d}^2\phi}{\mathrm{d}\eta^2}\mathrm{Nd}=0, \tag{20}$$

$$\frac{\mathrm{d}^2 \phi}{\mathrm{d}\eta^2}+\frac{3}{4}f\frac{\mathrm{d}\phi}{\mathrm{d}\eta}\mathrm{Le}+\frac{\mathrm{d}^2\theta}{\mathrm{d}\eta^2}\mathrm{Ld}=0, \tag{21}$$

$$\frac{\mathrm{d}^2 \gamma}{\mathrm{d}\eta^2}+\frac{3}{4}f\frac{\mathrm{d}\gamma}{\mathrm{d}\eta}\mathrm{Ln}+\frac{\mathrm{d}^2\theta}{\mathrm{d}\eta^2}\frac{\mathrm{Nt}}{\mathrm{Nb}}=0, \tag{22}$$

$$\begin{aligned}&f(0)=0, \theta(0)=1, \phi(0)=1, \gamma(0)=1, f'(0)=0 \text{ at } \eta=0,\\ &f'(\eta)\rightarrow 0,\ \gamma(\eta)\rightarrow 0,\ \ \phi(\eta)\rightarrow 0,\ \ \theta(\eta)\rightarrow 0, \text{ as } \ \eta\rightarrow\infty.\end{aligned} \tag{23}$$

3 Solution methodology

The solution methodology is comprised of two steps: Firstly, the reference data set of LMS–BPNN is generated by solving transformed ODEs system presented in Eqs. (19)–(23) via Lobatto-IIIA numerical solver in MATLAB using "bvp4c" package by variation of magnetic field parameter (M), thermal Grashof number (Gr), angle of inclination (α), Brownian motion parameter (Nb), Dufour-solutal Lewis number (Ld), modified Dufour parameter (Nd) and thermophoresis parameter (Nt). Later on, the designed AI-based Levenberg–Marquardt scheme with backpropagated neural network (LMS–BPNN) is implemented with the help of MATLAB command 'ftool' which is an artificial neural network (ANN) toolbox.

The 'nftool' command is utilized to examine the MSE results, histogram studies and regression analysis that validates the performance of LMS–BPNN of the proposed DDFC-NFM. The solution for $f'(\eta), \theta(\eta), \phi(\eta)$ and $\gamma(\eta)$ for input 0 to 10 is randomly dispersed, and the reference data set is segmented to generate a set for training data (80%), validation data (10%) and testing data (10%) to operate the designed LMS–BPNN. The proposed LMS–BPNN is presented as an artificial neural network in Fig. 2, and a flowchart of methodology is depicted in Fig. 3.

4 Analysis and discussion of result

The designed LMS–BPNN is operated under the influence of parameters of interest Gr, α, M, Ld, Nb, Nd and Nt for DDFC-NFM. There are seven scenarios each with four cases. Table 1 shows the numerical values of parameters of interest associated with DDFC-NFM which are used in the rest of work. Figures 4 and 5 show the performance and transition state of the proposed LMS–BPNN, while Figs. 6, 7 and 8 show the fitness curve with error analysis for scenarios 1–3, 4–6 and 7, respectively. Figures 9 and 10 show the regression of DDFC-NFM for scenarios 1–4 and 5–7 by LMS–BPNN, respectively. Furthermore, the MSE convergence for performance of training, testing and validation, performance, epochs, backpropagated operator, i.e., Mu, and time taken are depicted in Table 2.

The convergence curves of MSE for the second case of all seven scenarios of DDFC-NFM are represented in Fig. 4(I)–(VII) for training, testing and validation. The excellent or best curves are achieved at 654, 234, 111, 166, 219, 215 and 141 epochs, while MSE is almost $10^{-9}, 10^{-9}\rightarrow 10^{-7}, 10^{-10}\rightarrow 10^{-9}, 10^{-10}\rightarrow 10^{-9}, 10^{-10}\rightarrow 10^{-9}, 10^{-9}, 10^{-9}\rightarrow 10^{-8}$, respectively. The values of gradient and MU parameter for LMS–BPNN are shown in Fig. 5(I)–(VII). These values are $[\ 9.99\times10^{-8}, 9.95\times10^{-8}, 9.99\times10^{-8}, 9.95\times10^{-8}, 9.94\times10^{-8}, 9.96\times10^{-8}, 9.98\times10^{-8}, 9.99\times10^{-8}, 9.81\times10^{-8}]$ and $[10^{-09}, 10^{-09}, 10^{-09}, 10^{-09}, 10^{-09}, 10^{-08}, 10^{-08}]$. The validation and efficient convergence of LMS–BPNN for each case of DDFC-NFM have been proved by the outcomes.

The comparative study for LMS–BPNN outcomes with the reference data solution is presented in Fig. 6(I–VI) for scenarios 1–3, Fig. 7(I–VI) for scenarios 4–9 and Fig. 8,

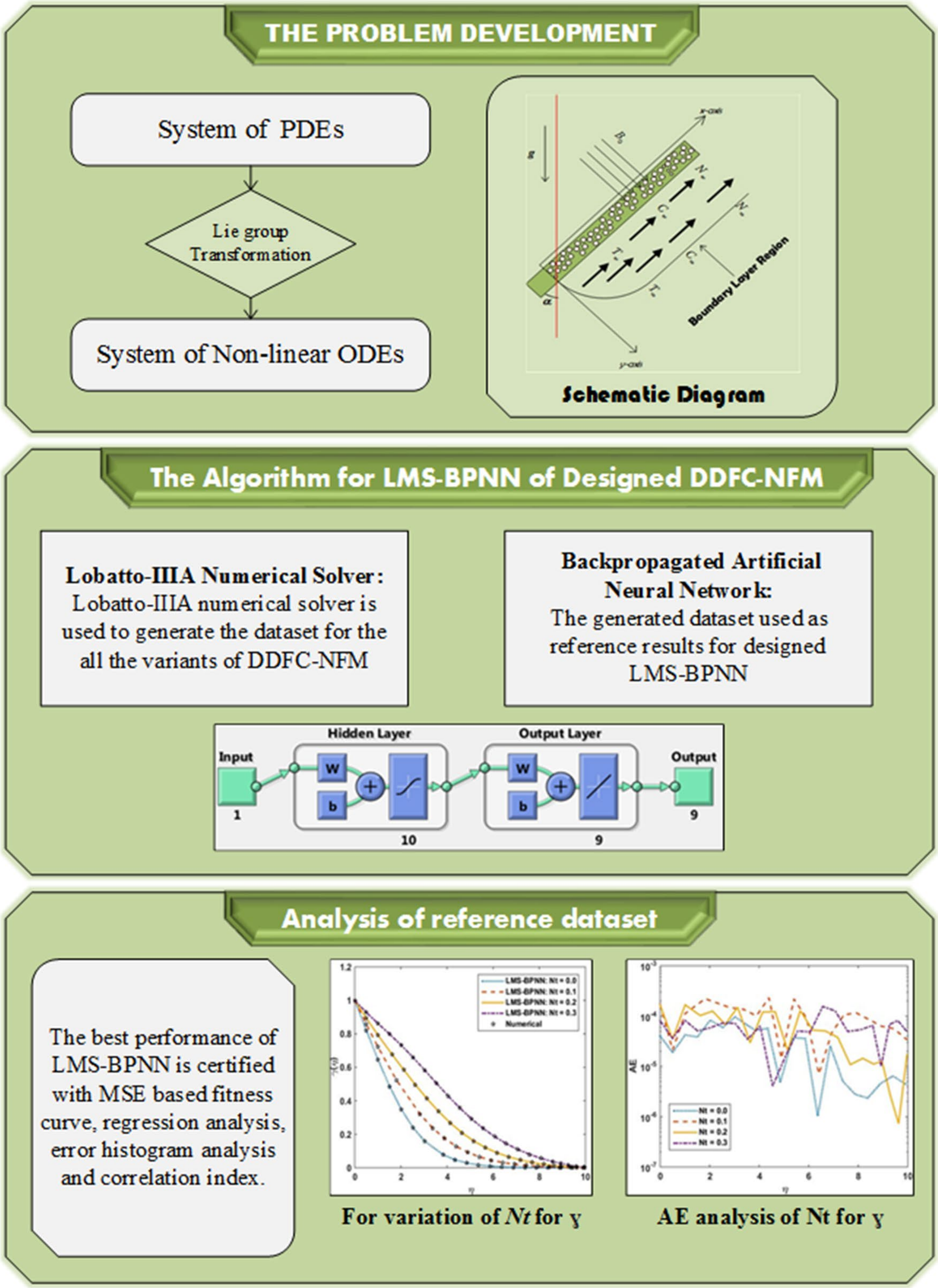

Fig. 3 The neural network for DDFC-NFM

Table 1 Depiction for all scenarios of DDFC-NFM

Scenario	Cases	Physical quantities						
		Gr	α	M	Ld	Nb	Nd	Nt
1	1	1.0	$\pi/6$	0.5	1.0	0.2	0.3	0.3
	2	2.0	$\pi/6$	0.5	1.0	0.2	0.3	0.3
	3	3.0	$\pi/6$	0.5	1.0	0.2	0.3	0.3
	4	4.0	$\pi/6$	0.5	1.0	0.2	0.3	0.3
2	1	1.0	0	0.5	1.0	0.2	0.3	0.3
	2	1.0	$\pi/6$	0.5	1.0	0.2	0.3	0.3
	3	1.0	$\pi/4$	0.5	1.0	0.2	0.3	0.3
	4	1.0	$\pi/3$	0.5	1.0	0.2	0.3	0.3
3	1	1.0	$\pi/6$	0.5	1.0	0.2	0.3	0.3
	2	1.0	$\pi/6$	1.5	1.0	0.2	0.3	0.3
	3	1.0	$\pi/6$	2.5	1.0	0.2	0.3	0.3
	4	1.0	$\pi/6$	3.5	1.0	0.2	0.3	0.3
4	1	1.0	$\pi/6$	0.5	0.2	0.2	0.3	0.3
	2	1.0	$\pi/6$	0.5	0.6	0.2	0.3	0.3
	3	1.0	$\pi/6$	0.5	1.0	0.2	0.3	0.3
	4	1.0	$\pi/6$	0.5	1.2	0.2	0.3	0.3
5	1	1.0	$\pi/6$	0.5	1.0	1.0	0.3	0.3
	2	1.0	$\pi/6$	0.5	1.0	1.5	0.3	0.3
	3	1.0	$\pi/6$	0.5	1.0	2.5	0.3	0.3
	4	1.0	$\pi/6$	0.5	1.0	3.5	0.3	0.3
6	1	1.0	$\pi/6$	0.5	1.0	0.2	0.0	0.3
	2	1.0	$\pi/6$	0.5	1.0	0.2	0.5	0.3
	3	1.0	$\pi/6$	0.5	1.0	0.2	1.0	0.3
	4	1.0	$\pi/6$	0.5	1.0	0.2	1.5	0.3
7	1	1.0	$\pi/6$	0.5	1.0	0.2	0.3	0.0
	2	1.0	$\pi/6$	0.5	1.0	0.2	0.3	0.1
	3	1.0	$\pi/6$	0.5	1.0	0.2	0.3	0.2
	4	1.0	$\pi/6$	0.5	1.0	0.2	0.3	0.3

which are further validated by error analysis. The information about correlation can be examined by the investigation of regression analysis. The regression plots are given in Figs. 9(I)–(IV) and 10(I)–(III) for scenarios 1–4 and 5–7 of DDFC-NFM, respectively. The value closure to unity of correlation R proved the perfection of modeling, in terms of training, testing and validation endorsed the effectiveness of LMS–BPNN for the designed DDFC-NFM.

Moreover, the total numerical analysis for all seven scenarios is shown in Table 2. The performance measures of LMS–BPNN for all cases of scenario lie in the range $10^{-9}, 10^{-10} \rightarrow 10^{-9}$ for all corresponding cases of scenario 2. Moreover, for scenarios 3–7 the performances are $10^{-10} \rightarrow 10^{-8}, 10^{-10} \rightarrow 10^{-9}, 10^{-10} \rightarrow 10^{-9}, 10^{-10} \rightarrow 10^{-9}$ and 10^{-9}, respectively, for the designed DDFC-NFM. In Table 2, the precise and accurate performance of LMS–BPNN is certified by numerical illustrations for solving each variant of DDFC-NFM.

4.1 Impact on velocity profile $f'(\eta)$ and absolute error analysis

The MATLAB software is used to analyze the results of LMS–BPNN for investigating the effects of variation of thermal Grashof number (Gr), angle of inclination (α) and magnetic field parameter (M) of velocity profile $f'(\eta)$ with absolute errors as depicted in Fig. 11. Figure 11a depicts the impact of thermal Grashof number on $f'(\eta)$ with an absolute error about $10^{-6} \rightarrow 10^{-3}$ as shown in Fig. 11b, while Fig. 11c represents the impact of angle of inclination on $f'(\eta)$ with an absolute error about $10^{-7} \rightarrow 10^{-2}$ as shown in Fig. 11d. Similarly, Fig. 11e depicts the influence of M on $f'(\eta)$ with an absolute error about $10^{-7} \rightarrow 10^{-3}$ as shown in Fig. 11f.

One may notice that

Table 2 Comparative study through backpropagation networks for all scenarios associated with DDFC-NFM

Sc	C	MSE levels			Best perform	Gradient	Mu	Ep	Time (s)
		Training	Validation	Testing					
1	1	1.30E−09	2.00E−09	1.90E−09	1.30E−09	9.93E−08	1E−09	137	8
	2	1.65E−09	1.71E−09	2.47E−09	1.65E−09	9.99E−08	1E−09	654	59
	3	1.04E−09	1.26E−09	1.17E−09	1.04E−09	9.95E−08	1E−09	929	89
	4	7.02E−09	1.01E−08	5.12E−09	7.02E−09	9.92E−08	1E−09	342	35
2	1	4.27E−09	5.37E−09	4.18E−09	4.27E−09	9.62E−08	1E−09	203	17
	2	4.83E−09	3.51E−08	6.33E−09	4.83E−09	9.95E−08	1E−08	234	15
	3	1.69E−09	1.94E−09	1.86E−09	1.69E−09	9.99E−08	1E−09	239	48
	4	4.41E−10	5.27E−10	5.01E−10	4.41E−10	9.91E−08	1E−09	119	10
3	1	2.79E−09	6.58E−09	4.10E−09	2.79E−09	9.71E−08	1E−09	236	79
	2	4.12E−10	4.26E−10	4.17E−10	4.12E−10	9.94E−08	1E−09	111	7
	3	2.86E−10	6.47E−10	2.86E−10	9.93E−08	9.93E−08	1E−09	118	9
	4	3.94E−09	4.49E−09	6.08E−09	3.94E−09	9.86E−08	1E−08	167	11
4	1	5.23E−10	6.27E−10	6.09E−10	5.23E−10	9.98E−08	1E−09	120	12
	2	8.64E−10	9.46E−10	6.75E−10	8.64E−10	9.96E−08	1E−09	166	13
	3	7.01E−10	7.47E−10	9.30E−10	7.01E−10	9.88E−08	1E−09	168	11
	4	1.21E−09	1.96E−09	2.37E−09	1.21E−09	9.91E−08	1E−09	130	8
5	1	8.64E−10	2.37E−09	1.93E−09	8.64E−10	9.98E−08	1E−09	386	25
	2	1.36E−09	4.71E−09	1.42E−09	1.36E−09	9.98E−08	1E−09	219	17
	3	1.10E−09	1.53E−09	1.81E−09	1.10E−09	9.87E−08	1E−09	690	50
	4	2.25E−09	2.37E−09	2.72E−09	2.25E−09	9.94E−08	1E−09	521	36
6	1	4.99E−10	5.85E−10	5.31E−10	4.99E−10	9.95E−08	1E−09	517	47
	2	3.93E−09	4.26E−09	5.00E−09	3.93E−09	9.99E−08	1E−08	215	33
	3	4.16E−09	4.99E−09	5.52E−09	4.16E−E−09	9.85E−08	1E−08	192	26
	4	3.10E−09	3.02E−09	3.87E−09	3.10E−09	9.93E−08	1E−09	262	25
7	1	3.44E−09	4.99E−09	4.56E−09	3.44E−09	9.92E−08	1E−08	188	15
	2	8.62E−09	8.26E−09	8.57E−09	8.62E−09	9.81E−08	1E−08	141	4
	3	4.95E−E−09	5.91E−09	5.85E−09	4.95E−09	9.93E−08	1E−08	243	20
	4	4.46E−09	4.94E−09	4.29E−09	4.46E−09	9.96E−08	1E−08	246	27

- The velocity enhances swiftly near the surface with the rise in Gr and then gradually decreases and approaches to zero as $\eta \to \infty$. This is due to the fact that the Gr is the ratio of thermal buoyancy force to viscous hydrodynamic force in the boundary layer. So, the increment in the Gr causes an increment in thermal buoyancy force in the system, which weakens the bonds between fluids and consequently lowers the internal friction pressure and increases the gravity [59].
- The velocity $f'(\eta)$ decays with the increase in M due to the fact that a retarding force is exerted by magnetic field on free convection flow.
- The velocity $f'(\eta)$ declines with the increase in α. As angle of inclination α increases, the effect of buoyancy force decreases due to thermal diffusion.

4.2 Impact on temperature profile $\theta(\eta)$ and absolute error analysis

The MATLAB software is used to analyze the results of LMS–BPNN for investigating the impact of change in Brownian motion parameter (Nb), modified Dufour parameter (Nd) and thermophoresis parameter (Nt) of temperature profile $\theta(\eta)$ with absolute errors as illustrated in Fig. 12. Figure 12a depicts the Brownian motion parameter impact on $\theta(\eta)$ with an absolute error about $10^{-7} \to 10^{-3}$ (Fig. 12b), while the effect of the modified Dufour parameter on $\theta(\eta)$ with an absolute error about $10^{-7} \to 10^{-4}$ is shown in Fig. 12c, d. Similarly, Fig. 12e represents the impact of thermophoresis parameter on $\theta(\eta)$ with an absolute error about $10^{-7} \to 10^{-3}$ as shown in Fig. 12f.

One may notice that

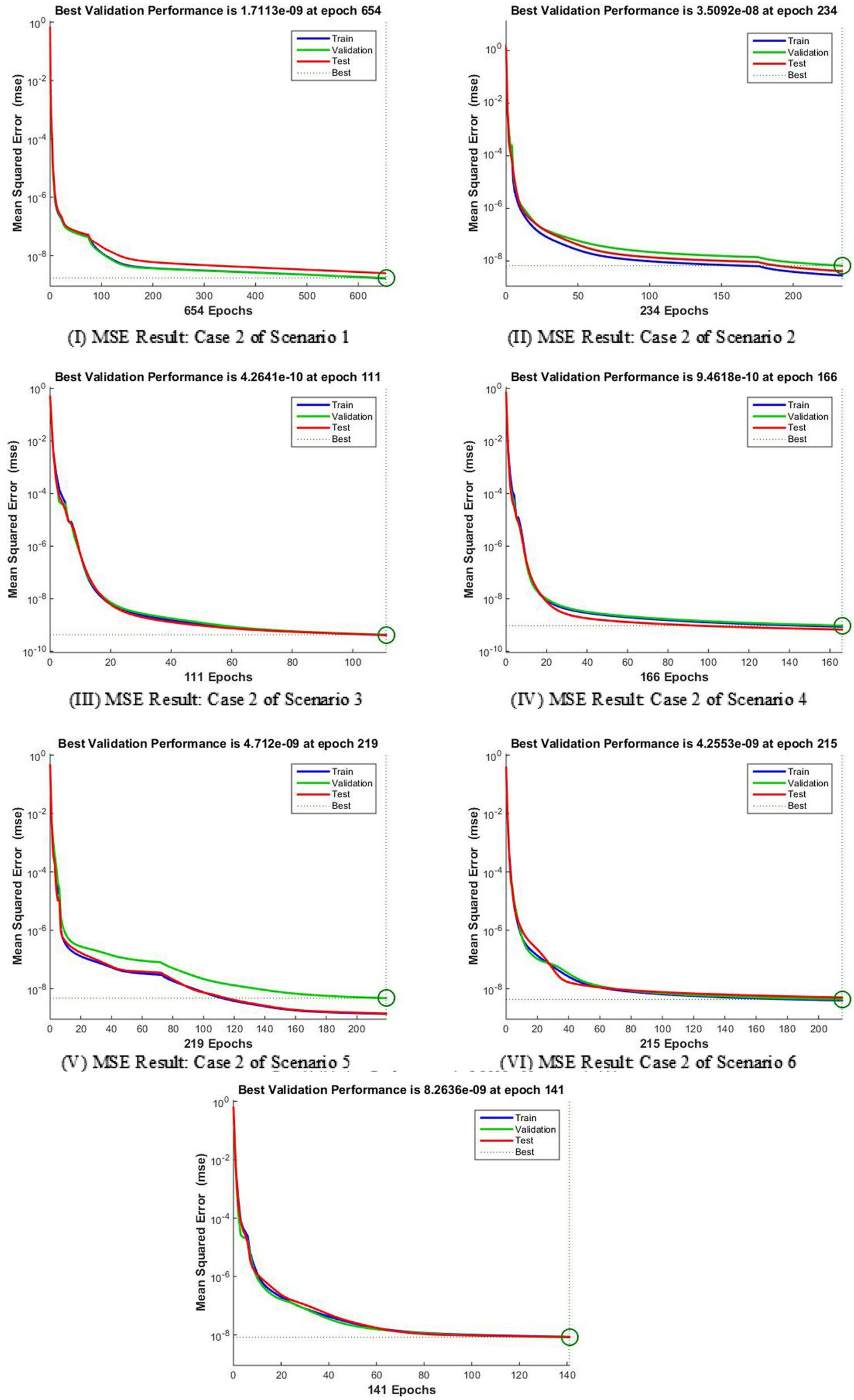

(I) MSE Result: Case 2 of Scenario 1

(II) MSE Result: Case 2 of Scenario 2

(III) MSE Result: Case 2 of Scenario 3

(IV) MSE Result Case 2 of Scenario 4

(V) MSE Result: Case 2 of Scenario 5

(VI) MSE Result Case 2 of Scenario 6

(VII) MSE Result Case 2 of Scenario 7

Fig. 4 The neural network for DDFC-NFM

Fig. 5 Transition state of LMS–BPNN of case 2 of all the scenarios of DDFC-NFM

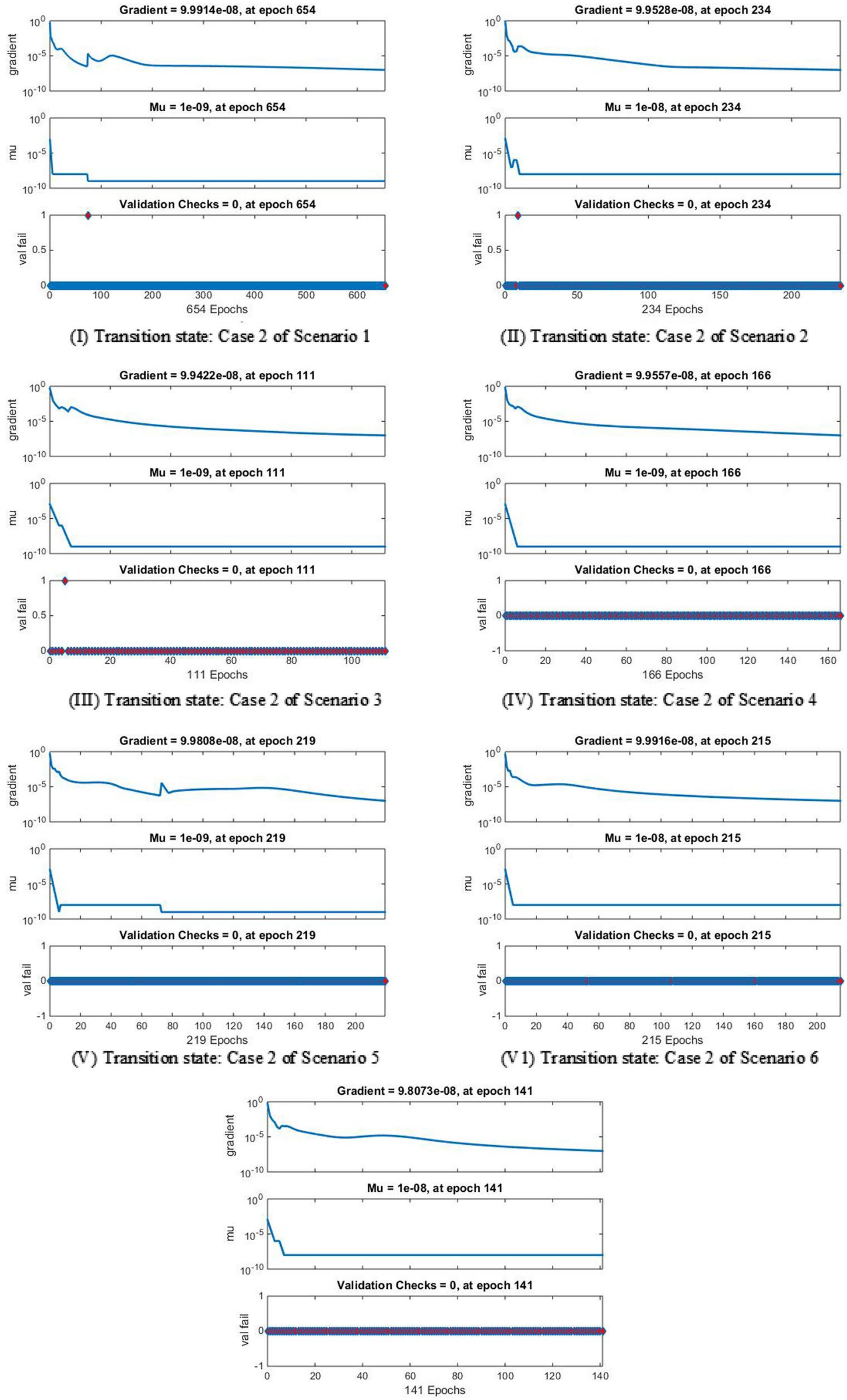

(I) Transition state: Case 2 of Scenario 1

(II) Transition state: Case 2 of Scenario 2

(III) Transition state: Case 2 of Scenario 3

(IV) Transition state: Case 2 of Scenario 4

(V) Transition state: Case 2 of Scenario 5

(VI) Transition state: Case 2 of Scenario 6

(VII) Transition state: Case 2 of Scenario 7

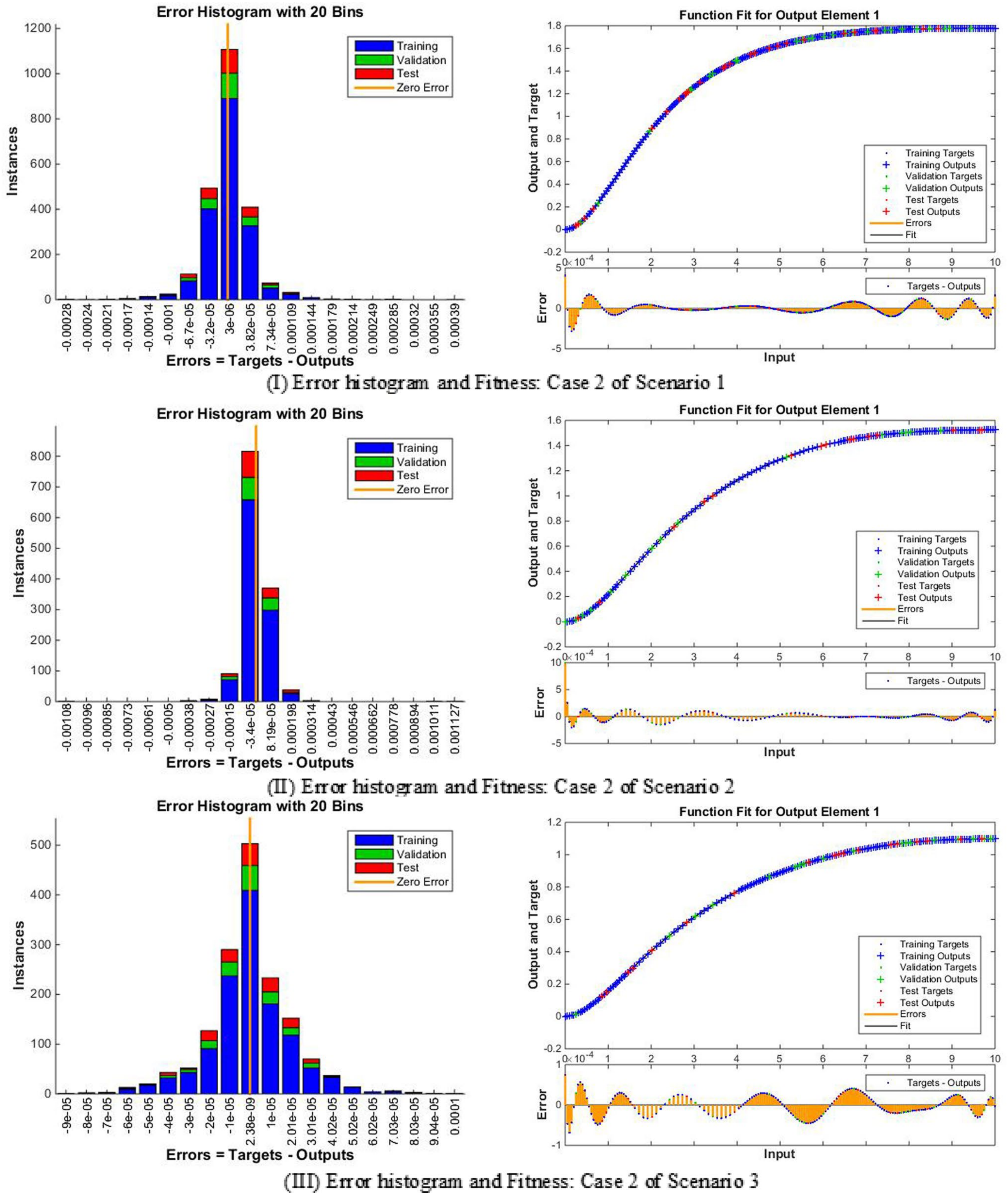

Fig. 6 Error analysis and fitness of function for the designed LMS–BPNN of case 2 of scenarios 1–3 of DDFC-NFM

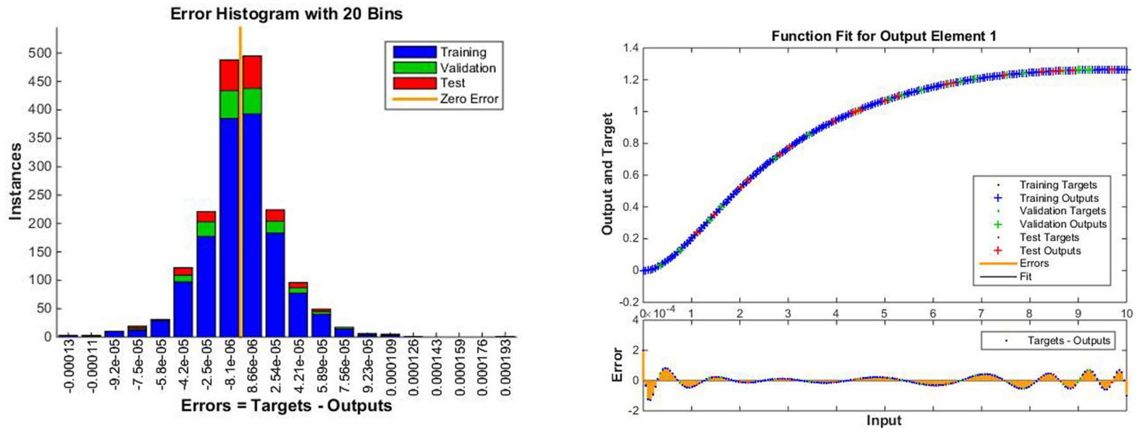

(I) Error histogram and Fitness: Case 2 of Scenario 4

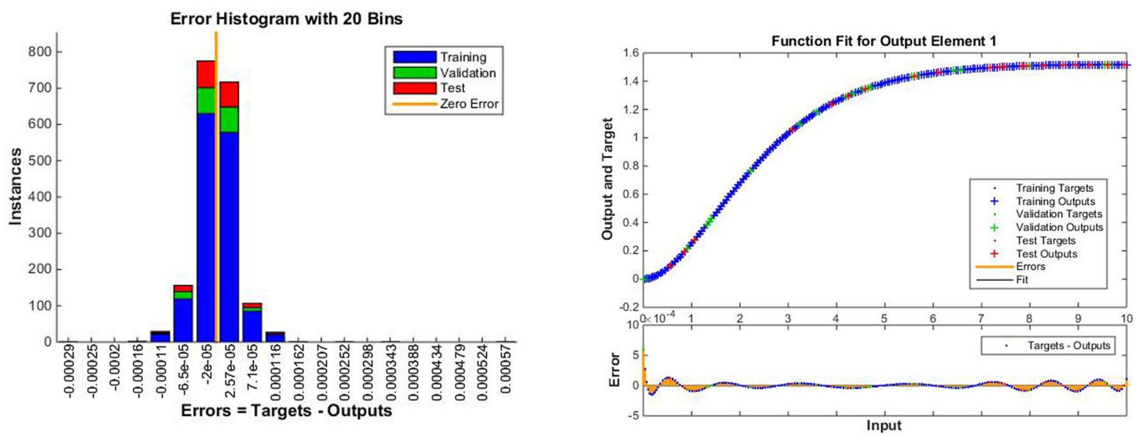

(II) Error histogram and Fitness: Case 2 of Scenario 5

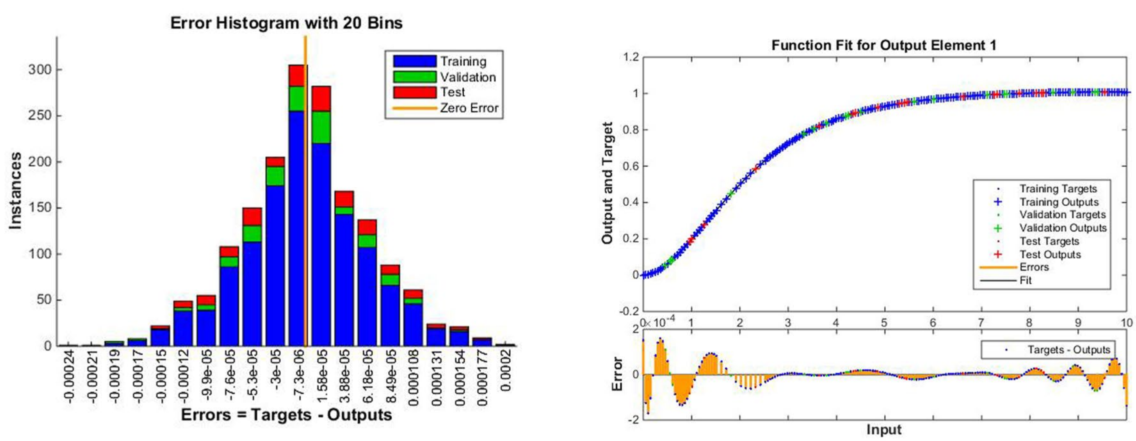

(III) Error histogram and Fitness: Case 2 of Scenario 6

Fig. 7 Error analysis and fitness of function for the designed LMS–BPNN of case 2 of scenarios 4–6 of DDFC-NFM

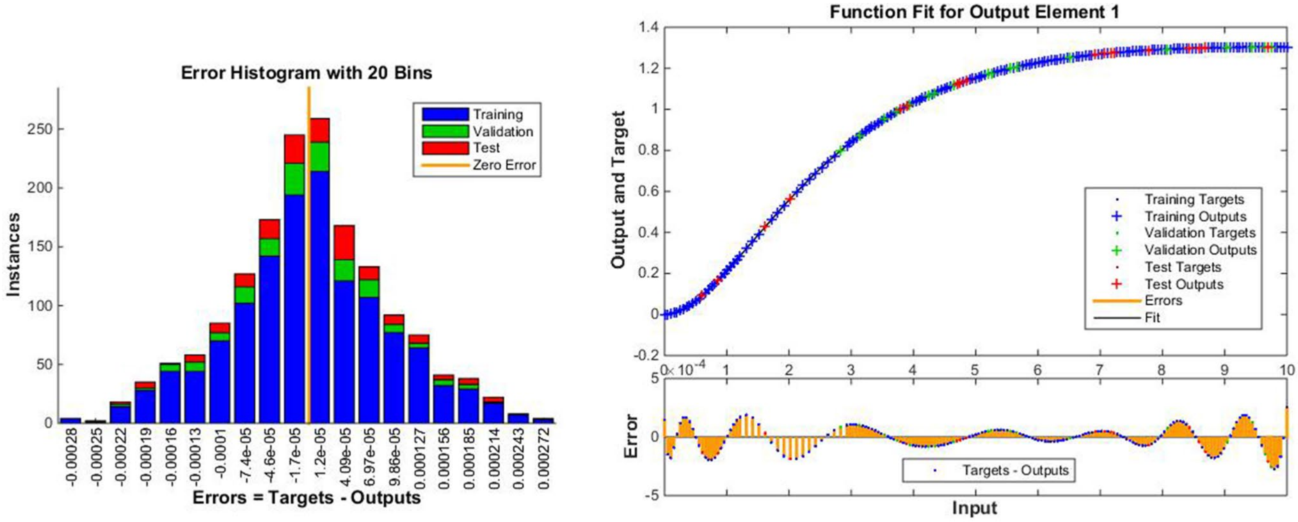

Fig. 8 Error analysis and fitness of function for the designed LMS–BPNN of case 2 of scenario 7 of DDFC-NFM

- The $\theta(\eta)$ profile enhances with the increment in the values of Brownian motion parameter (Nb), modified Dufour parameter (Nd) and thermophoresis parameter (Nt). When the *Nt*, *Nb* and Nd increase, the thermal boundary layer expands. In a recent meta-analysis, it was concluded that due to Brownian motion of nanoparticles internal pressure of nanoparticles increases and as a result temperature increases [60]. Another study [61] reveals that the different reactions to a temperature gradient's force are adequate to improve the temperature profile due to increased thermophoresis.

4.3 Impact on solutal concentration profile $\phi(\eta)$ and absolute error analysis

The MATLAB software is used to analyze the results of LMS–BPNN for investigating the impact of variation of Dufour-solutal Lewis number (Ld) and modified Dufour parameter (Nd) on $\phi(\eta)$ with absolute errors as depicted in Fig. 13. Figure 13a shows the effect of Ld on $\phi(\eta)$ with an absolute error about $10^{-7} \to 10^{-4}$ as shown in Fig. 13b, while the impact of Nd on $\phi(\eta)$ with an absolute error about $10^{-7} \to 10^{-3}$ is shown in Fig. 13c, d.

One may notice that

- The $\phi(\eta)$ profile increases with an increment in the value of Ld, which occurs for Newtonian fluid. The effect is prominent around the boundary-layer region, i.e., $\eta \leq 6$; afterward, it gradually converges. Increasing regular Lewis number implies increasing thermal diffusion so the solute concentration velocity increases and gets the tendency to scatter away from boundary-layer region; as a consequence, solute concentration boundary-layer thickness declines. But, the opposite behavior is seen in case of Ld.
- The increase in the modified Dufour parameter causes a decrease in solutal concentration profile.

4.4 Impact on nanoparticle volume fraction profile $\gamma(\eta)$ and absolute error analysis

The MATLAB software is used to analyze the results of LMS–BPNN for investigating the impact of variation of thermophoresis parameter (Nt) and Brownian motion parameter Nb on $\gamma(\eta)$ with absolute errors as depicted in Fig. 14. Figure 14a shows the impact of Nb on $\gamma(\eta)$ with an absolute error about $10^{-7} \to 10^{-3}$ as shown in Fig. 14b, while Fig. 14c represents the effect of Nt on $\gamma(\eta)$ with an absolute error about $10^{-7} \to 10^{-3}$ as shown in Fig. 14d.

One may reveal that:

- Nanoparticle volume friction profile decreases, that is, boundary-layer thickness decreases with the enhancement of Nb.
- The prominent and opposite effect is seen; as the value of Nt increases, the enhancement of nanoparticle volume frictions occurs. This is due to increasing diffusivity as increase in thermophoresis because particles move from hot to cold so there is an enhancement of density of nanoparticles within boundary layer.

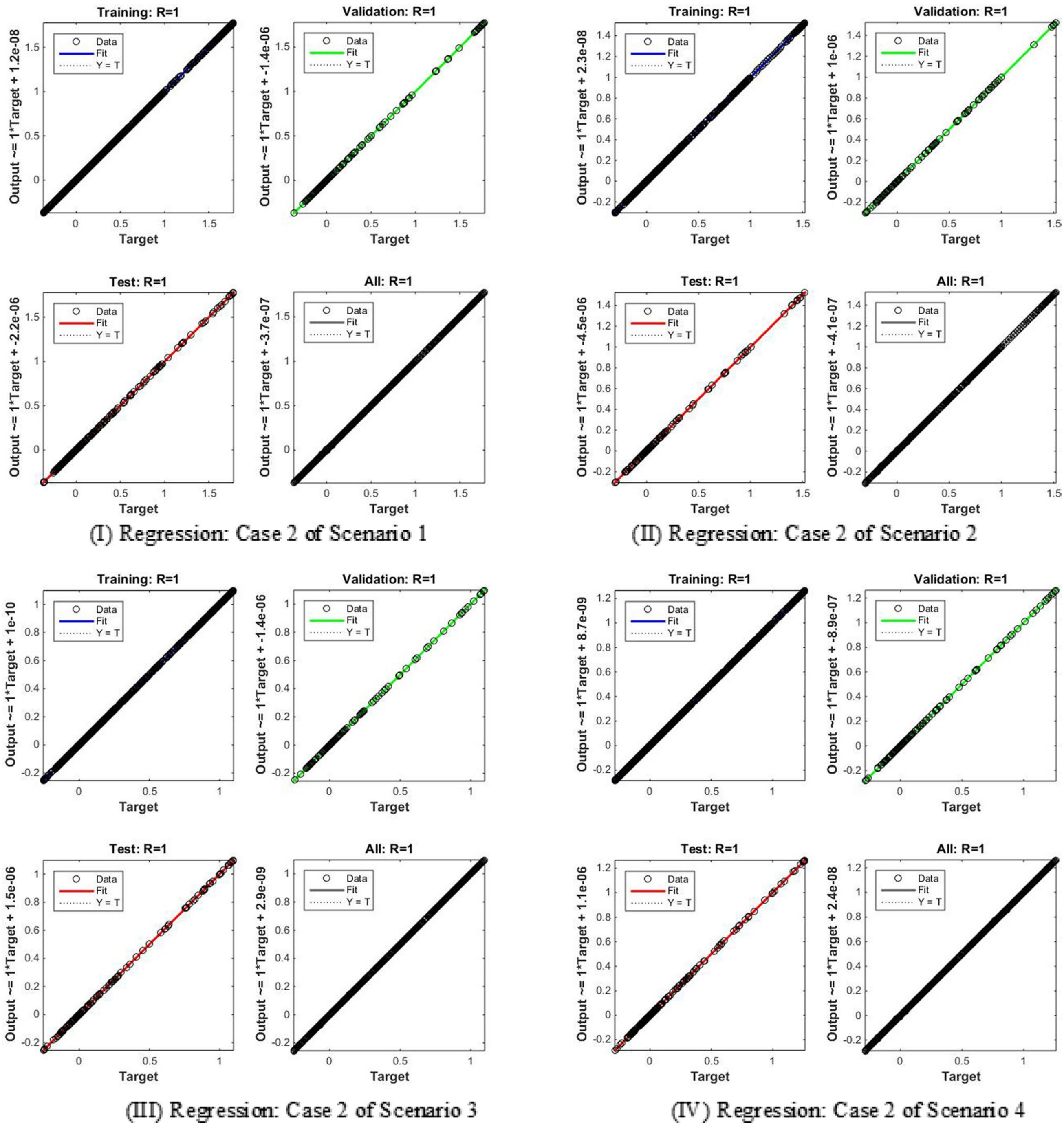

Fig. 9 Regression illustrations for the designed LMS–BPNN result for case 2 of scenarios 1–4 of DDFC-NFM

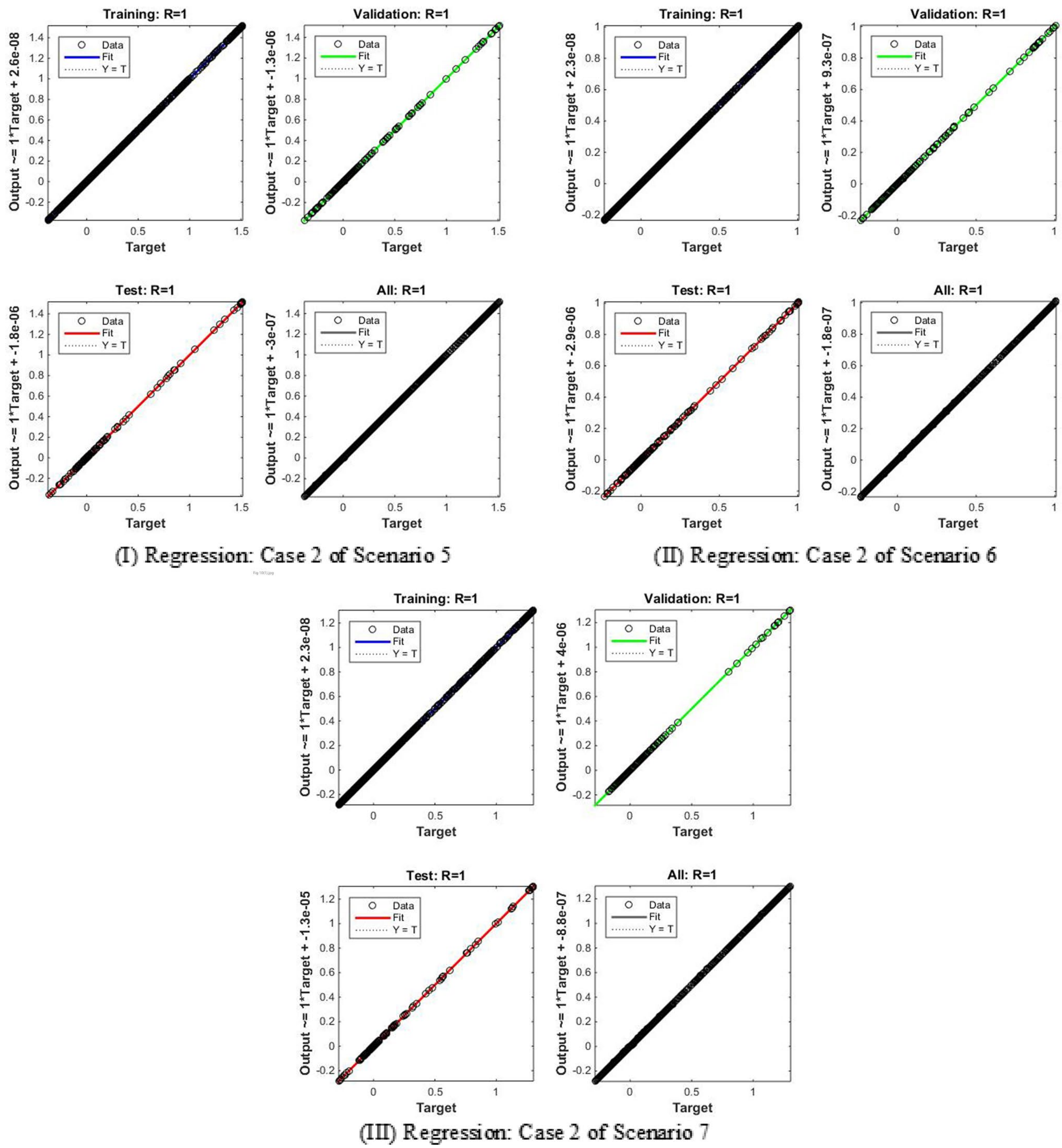

Fig. 10 Regression illustrations for the designed LMS–BPNN result for case 2 of scenarios 5–7 of DDFC-NFM

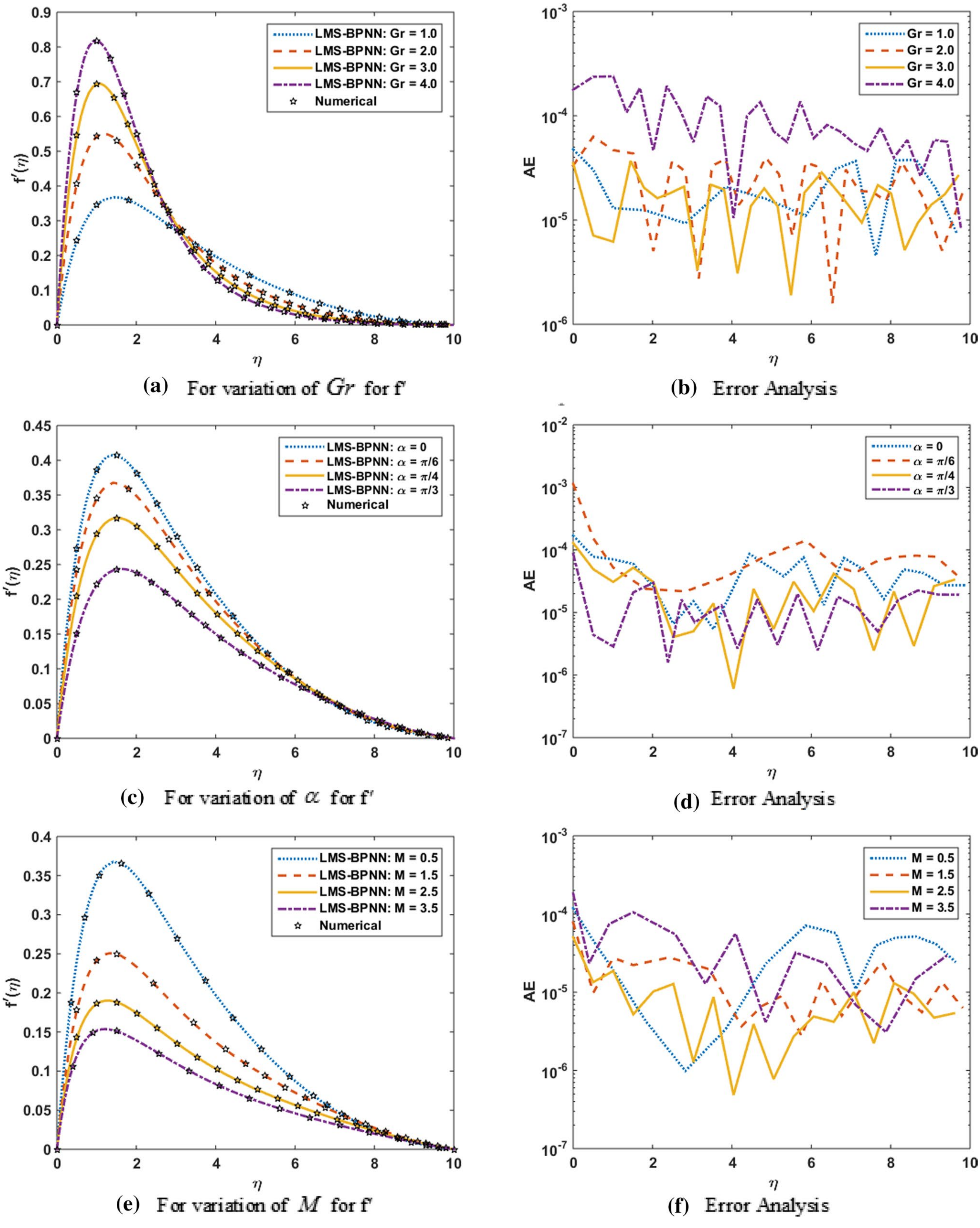

Fig. 11 Assessment of LMS–BPNN for $f'(\eta)$ with reference data set of DDFC-NFM

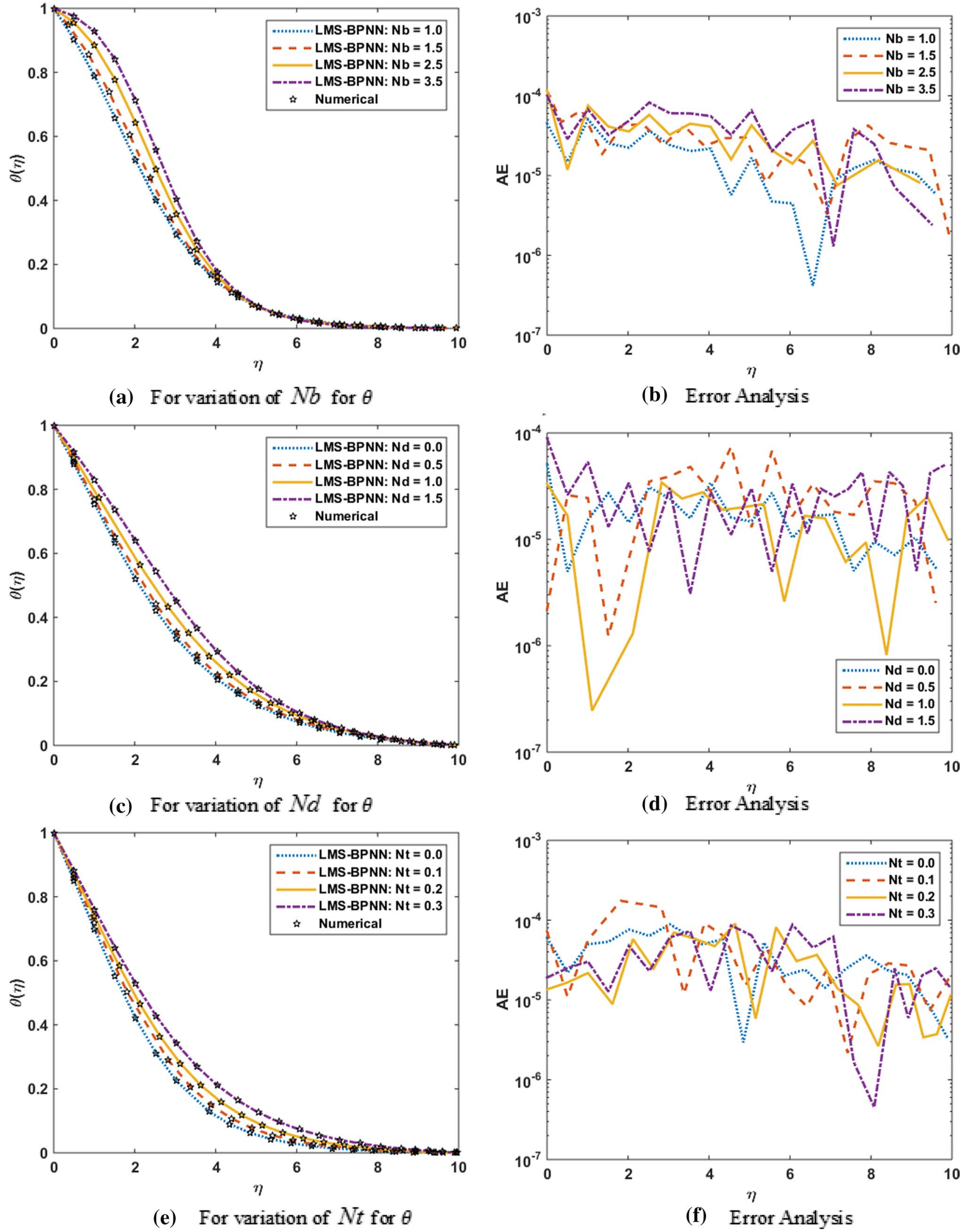

(a) For variation of Nb for θ

(b) Error Analysis

(c) For variation of Nd for θ

(d) Error Analysis

(e) For variation of Nt for θ

(f) Error Analysis

Fig. 12 Assessment of LMS–BPNN for $\theta(\eta)$ with reference data set of DDFC-NFM

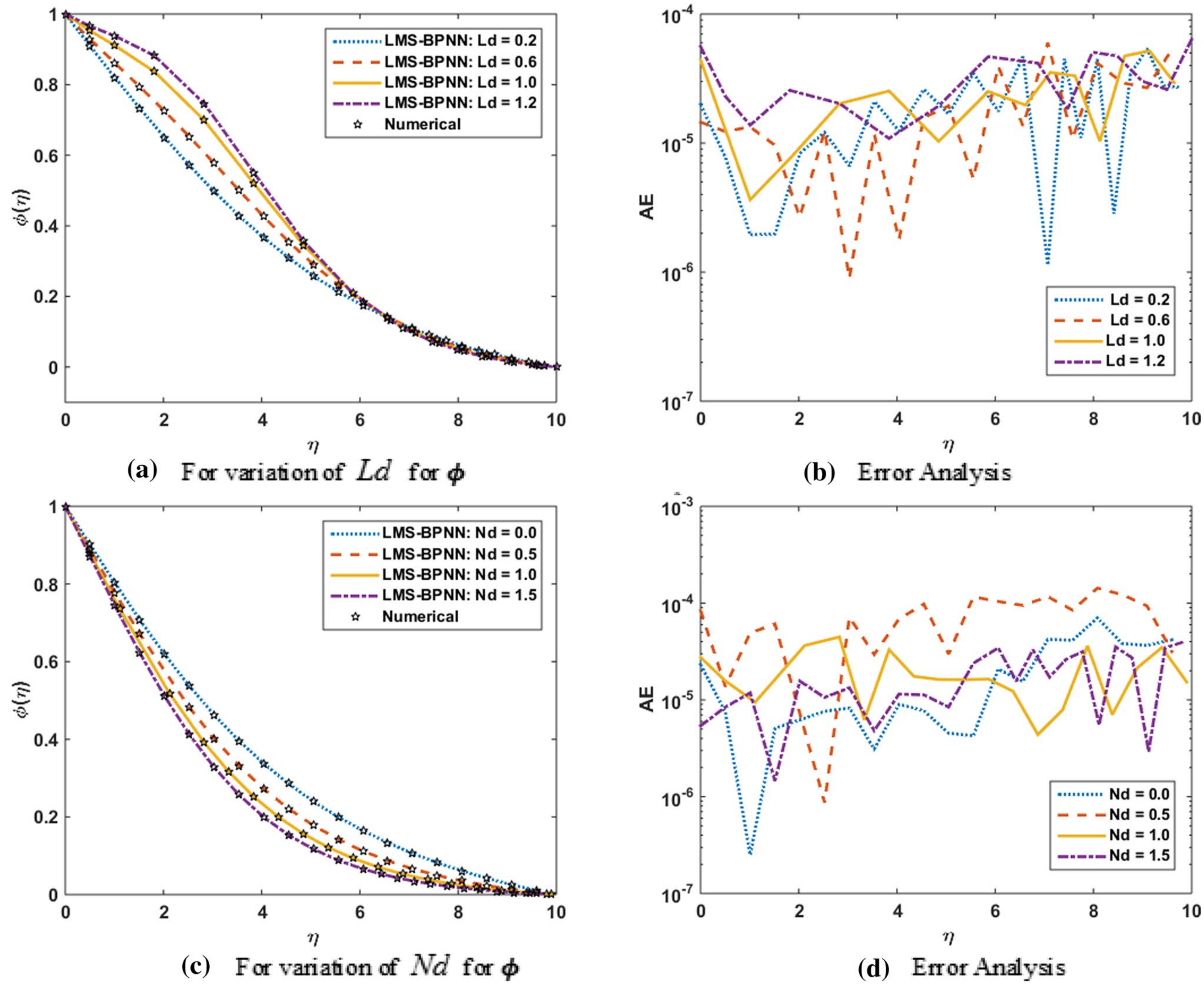

Fig. 13 Assessment of LMS–BPNN for $\phi(\eta)$ with reference data set of DDFC-NFM

5 Conclusion

The technique of AI-based Levenberg–Marquardt scheme with backpropagated neural network (LMS–BPNN) had been used to analyze the problem of double-diffusive flow of nanofluid (DDFC-NFM) due to free convection over an inclined plane when Brownian motion and thermophoresis of tiny particles as the fluid flows through a porous medium are significant. The governing PDEs representing DDFC-NFM are transformed into system of nonlinear ODEs by applying suitable transformation. The reference data set is generated from Lobatto III-A numerical solver by variation of magnetic field parameter (M), thermal Grashof number (Gr), angle of inclination (α), Brownian motion parameter (Nb), Dufour-solutal Lewis number (Ld), modified Dufour parameter (Nd) and thermophoresis parameter (Nt). The data sets as reference results are executed for training data (80%) validation data (10%) and testing data (10%) by operating LMS–BPNN solver. The proposed and reference outcomes verify the correctness of technique and are further endorsed through numerical and graphical illustration of mean square

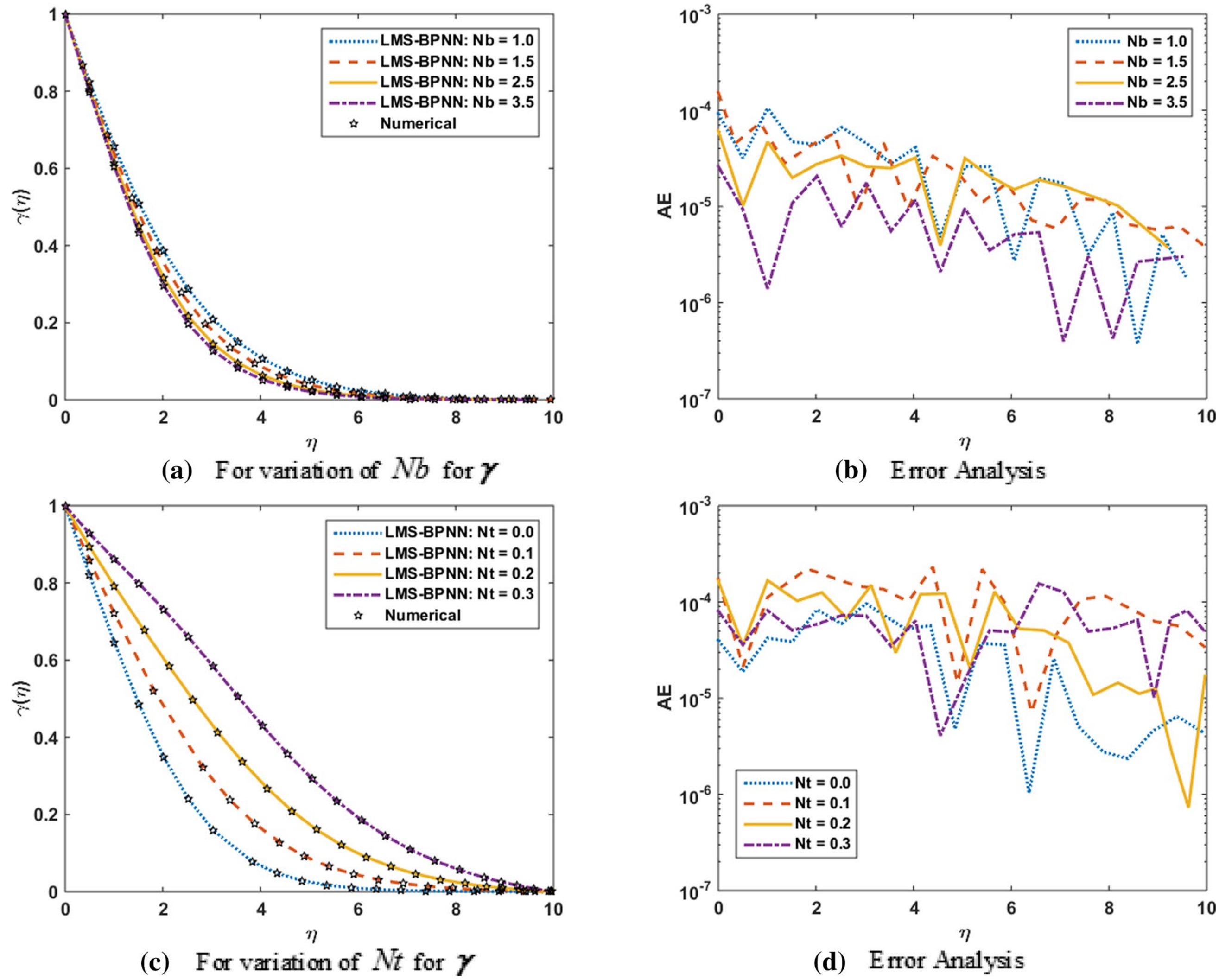

Fig. 14 Assessment of LMS–BPNN for $\gamma(\eta)$ with reference data set of DDFC-NFM

error convergence plots, correlation regression analysis and histogram studies.

It is concluded that:

- The velocity increases with the increment in Gr.
- When the values of angle of inclination and magnetic field parameter increase, velocity profile decreases.
- The temperature profile increases with the increase in Nb, Nd and Nt.
- The solutal concentration profile increases with the enhancement of Ld.
- The increase in the modified Dufour parameter causes a decrease in solutal concentration profile.
- When thermophoresis parameter increases, the enhancement of nanoparticle volume frictions occurs.
- The increase in Brownian motion parameter leads to a decrease in nanoparticle volume frictions.

In future, one may work on different nanofluidic models [62–65] to solve a problem through backpropagated neural networks.

Acknowledgements None.

Funding No funding is available for the present research.

Declarations

Conflict of interest All the authors of the manuscript declare that there is no conflict of interest.

References

1. Choi SU, Eastman JA (1995) Enhancing thermal conductivity of fluids with nanoparticles (No. ANL/MSD/CP-84938; CONF-951135-29). Argonne National Lab., IL (United States)
2. Khan I, Fatima S, Malik MY, Salahuddin T (2018) Exponentially varying viscosity of magnetohydrodynamic mixed convection Eyring-Powell nanofluid flow over an inclined surface. Res Phys 8:1194–1203
3. Zeeshan A, Ellahi R, Mabood F, Hussain F (2019) Numerical study on bi-phase coupled stress fluid in the presence of Hafnium and metallic nanoparticles over an inclined plane. Int J Numer Methods Heat Fluid Flow
4. Khademi R, Razminia A, Shiryaev VI (2020) Conjugate-mixed convection of nanofluid flow over an inclined flat plate in porous media. Appl Math Comput 366:124761
5. Rafique K, Anwar MI, Misiran M, Asjad MI (2020) Energy and mass transport of micropolar nanofluid flow over an inclined surface with Keller–Box simulation. Heat Transf 49(8):4592–4611
6. Idowu AS, Falodun BO (2020) Effects of thermophoresis, Soret–Dufour on heat and mass transfer flow of magnetohydrodynamics non-Newtonian nanofluid over an inclined plate. Arab J Basic Appl Sci 27(1):149–165
7. Animasaun IL, Yook SJ, Muhammad T, Mathew A (2022) Dynamics of ternary-hybrid nanofluid subject to magnetic flux density and heat source or sink on a convectively heated surface. Surf Interfaces 28:101654
8. Elnaqeeb T, Animasaun IL, Shah NA (2021) Ternary-hybrid nanofluids: significance of suction and dual-stretching on three-dimensional flow of water conveying nanoparticles with various shapes and densities. Zeitschrift für Naturforschung A 76(3):231–243
9. Krishna MV, Reddy GS (2018) MHD forced convective flow of non-Newtonian fluid through stumpy permeable porous medium. Mater Today Proc 5(1):175–183
10. Tlili I, Khan WA, Khan I (2018) Multiple slips effects on MHD SA-Al_2O_3 and SA-Cu non-Newtonian nanofluids flow over a stretching cylinder in porous medium with radiation and chemical reaction. Res Phys 8:213–222
11. Barnoon P, Toghraie D (2018) Numerical investigation of laminar flow and heat transfer of non-Newtonian nanofluid within a porous medium. Powder Technol 325:78–91
12. El-Zahar ER, Algelany AM, Rashad AM (2020) Sinusoidal natural convective flow of non-Newtonian nanoliquid over a radiative vertical plate in a saturated porous medium. IEEE Access 8:136131–136140
13. Kumar KA, Sugunamma V, Sandeep N, Reddy JR (2019) Numerical examination of MHD nonlinear radiative slip motion of non-newtonian fluid across a stretching sheet in the presence of a porous medium. Heat Transf Res 50(12)
14. Megahed AM (2021) Improvement of heat transfer mechanism through a Maxwell fluid flow over a stretching sheet embedded in a porous medium and convectively heated. Math Comput Simul 187:97–109
15. Khan M, Rasheed A, Salahuddin T, Ali S (2021) Chemically reactive flow of hyperbolic tangent fluid flow having thermal radiation and double stratification embedded in porous medium. Ain Shams Eng J
16. Riaz A, Zeeshan A, Bhatti MM, Ellahi R (2020) Peristaltic propulsion of Jeffrey nano-liquid and heat transfer through a symmetrical duct with moving walls in a porous medium. Phys A 545:123788
17. Yadav D (2021) The effect of viscosity and Darcy number on the start of convective motion in a rotating porous medium layer saturated by a couple-stress fluid. Proc Inst Mech Eng C J Mech Eng Sci 235(6):999–1007
18. Gebhart B, Pera L (1971) The nature of vertical natural convection flows resulting from the combined buoyancy effects of thermal and mass diffusion. Int J Heat Mass Transf 14(12):2025–2050
19. Murthy PVSN, Sutradhar A, RamReddy C (2013) Double-diffusive free convection flow past an inclined plate embedded in a non-Darcy porous medium saturated with a nanofluid. Transp Porous Media 98(3):553–564
20. Aly AM, Raizah ZA (2016) Double-diffusive natural convection in an enclosure filled with nanofluid using ISPH method. Alex Eng J 55(4):3037–3052
21. Hussain S, Mehmood K, Sagheer M, Yamin M (2018) Numerical simulation of double diffusive mixed convective nanofluid flow and entropy generation in a square porous enclosure. Int J Heat Mass Transf 122:1283–1297
22. Nag P, Molla MM (2021) February. Non-Newtonian effect on double diffusive natural convection of nanofluid within a square cavity. In: AIP conference proceedings, vol 2324, No 1, p 050030. AIP Publishing LLC
23. Said K, Ouadha A, Sabeur A (2020). CFD-based analysis of entropy generation in turbulent double diffusive natural convection flow in square cavity. In: MATEC web of conferences, vol 330. EDP Sciences
24. Raizah Z, Aly AM (2021) Double-diffusive convection of a rotating circular cylinder in a porous cavity suspended by nano-encapsulated phase change materials. Case Stud Therm Eng 24:100864
25. Prasad DK, Chaitanya GK, Raju RS (2019) Double diffusive effects on mixed convection Casson fluid flow past a wavy inclined plate in presence of Darcian porous medium. Res Eng 3:100019
26. Sailaja SV, Shanker B, Raju RS (2017) Double diffusive effects on MHD mixed convection Casson fluid flow towards a vertically inclined plate filled in porous medium in presence of Biot number: a finite element technique. J Nanofluids 6(3):420–435
27. Moolya S, Satheesh A (2020) Role of magnetic field and cavity inclination on double diffusive mixed convection in rectangular enclosed domain. Int Commun Heat Mass Transf 118:104814
28. Cheng CY (2012) Free convection boundary layer flow over a horizontal cylinder of elliptic cross section in porous media saturated by a nanofluid. Int Commun Heat Mass Transf 39(7):931–936
29. Uddin MJ, Khan WA, Ismail AM (2012) Free convection boundary layer flow from a heated upward facing horizontal flat plate embedded in a porous medium filled by a nanofluid with convective boundary condition. Transp Porous Media 92(3):867–881
30. Haddad Z, Abu-Nada E, Oztop HF, Mataoui A (2012) Natural convection in nanofluids: are the thermophoresis and Brownian motion effects significant in nanofluid heat transfer enhancement. Int J Therm Sci 57:152–162
31. Sheikholeslami M, Gorji-Bandpy M, Ganji DD, Rana P, Soleimani S (2014) Magnetohydrodynamic free convection of Al_2O_3–water nanofluid considering thermophoresis and Brownian motion effects. Comput Fluids 94:147–160
32. Sheikholeslami M, Chamkha AJ, Rana P, Moradi R (2017) Combined thermophoresis and Brownian motion effects on nanofluid free convection heat transfer in an L-shaped enclosure. Chin J Phys 55(6):2356–2370

33. Sheremet MA, Cimpean DS, Pop I (2017) Free convection in a partially heated wavy porous cavity filled with a nanofluid under the effects of Brownian diffusion and thermophoresis. Appl Therm Eng 113:413–418
34. Sobamowo MG, Yinusa AA, Makinde OD (2019) A study on the effects of inclined magnetic field, flow medium porosity and thermal radiation on free convection of Casson nanofluid over a vertical plate. World Sci News 138(1):1–64
35. Rafique K, Anwar MI, Misiran M, Khan I, Alharbi SO, Thounthong P, Nisar KS (2019) Numerical solution of Casson nanofluid flow over a non-linear inclined surface with Soret and Dufour effects by Keller–Box method. Front Phys 7:139
36. Bidemi OF, Ahamed MS (2019) Soret and Dufour effects on unsteady Casson magneto-nanofluid flow over an inclined plate embedded in a porous medium. World J Eng
37. Hosseinzadeh K, Afsharpanah F, Zamani S, Gholinia M, Ganji DD (2018) A numerical investigation on ethylene glycol-titanium dioxide nanofluid convective flow over a stretching sheet in presence of heat generation/absorption. Case Stud Therm Eng 12:228–236
38. Gholinia M, Hoseini ME, Gholinia S (2019) A numerical investigation of free convection MHD flow of Walters-B nanofluid over an inclined stretching sheet under the impact of Joule heating. Therm Sci Eng Progress 11:272–282
39. Parvin S, Mohamed Isa SSP, Arifin NM, Ali FM (2021) The inclined factors of magnetic field and shrinking sheet in Casson fluid flow. Heat Mass Transf Symmetry 13(3):373
40. Ahmad I, Raja MAZ, Bilal M, Ashraf F (2017) Neural network methods to solve the Lane–Emden type equations arising in thermodynamic studies of the spherical gas cloud model. Neural Comput Appl 28(1):929–944
41. Raja MAZ, Manzar MA, Shah FH, Shah FH (2018) Intelligent computing for Mathieu's systems for parameter excitation, vertically driven pendulum and dusty plasma models. Appl Soft Comput 62:359–372
42. Ahmad SI, Faisal F, Shoaib M, Raja MAZ (2020) A new heuristic computational solver for nonlinear singular Thomas–Fermi system using evolutionary optimized cubic splines. Eur Phys J Plus 135(1):1–29
43. Bukhari AH, Raja MAZ, Sulaiman M, Islam S, Shoaib M, Kumam P (2020) Fractional neuro-sequential ARFIMA-LSTM for financial market forecasting. IEEE Access 8:71326–71338
44. Awan SE, Raja MAZ, Gul F, Khan ZA, Mehmood A, Shoaib M (2021) Numerical computing paradigm for investigation of micropolar nanofluid flow between parallel plates system with impact of electrical MHD and hall current. Arab J Sci Eng 46(1):645–662
45. Sabir Z, Raja MAZ, Umar M, Shoaib M (2020) Design of neuro-swarming-based heuristics to solve the third-order nonlinear multi-singular Emden–Fowler equation. Eur Phys J Plus 135(5):410
46. Sabir Z, Raja MAZ, Guirao JL, Shoaib M (2020) Integrated intelligent computing with neuro-swarming solver for multi-singular fourth-order nonlinear Emden–Fowler equation. Comput Appl Math 39(4):1–18
47. Umar M, Sabir Z, Amin F, Guirao JL, Raja MAZ (2020) Stochastic numerical technique for solving HIV infection model of CD4+ T cells. Eur Phys J Plus 135(5):403
48. Ahmad I, Raja MAZ, Ramos H, Bilal M, Shoaib M (2020) Integrated neuro-evolution-based computing solver for dynamics of nonlinear corneal shape model numerically. Neural Comput Appl 33:5753–5769
49. Umar M, Raja MAZ, Sabir Z, Alwabli AS, Shoaib M (2020) A stochastic computational intelligent solver for numerical treatment of mosquito dispersal model in a heterogeneous environment. Eur Phys J Plus 135(7):1–23
50. Cheema TN, Raja MAZ, Ahmad I, Naz S, Ilyas H, Shoaib M (2020) Intelligent computing with Levenberg–Marquardt artificial neural networks for nonlinear system of COVID-19 epidemic model for future generation disease control. Eur Phys J Plus 135(11):1–35
51. Shoaib M, Raja MAZ, Sabir MT, Bukhari AH, Alrabaiah H, Shah Z, Kumam P, Islam S (2021) A stochastic numerical analysis based on hybrid NAR-RBFs networks nonlinear SITR model for novel COVID-19 dynamics. Comput Methods Programs Biomed 202:105973
52. Sivanandam Sivasankaran, Bhuvaneswari Marimuthu, Kandaswamy Palanigounder, Ramasami EK (2006) Lie group analysis of natural convection heat and mass transfer in an inclined surface. Nonlinear Anal Model Control 11:201–212
53. Reddy GM (2012) Lie group analysis of heat and mass transfer effects on steady MHD free convection dissipative fluid flow past an inclined porous surface with heat generation. Theor Appl Mech 39(3):233–254
54. Das K (2013) Lie group analysis for nanofluid flow past a convectively heated stretching surface. Appl Math Comput 221:547–557
55. Das K, Chakraborty T, Kundu PK (2019) Lie group transformation for double-diffusive free convection nanofluid flow over an inclined plane. Proc Natl Acad Sci India Sect A 89(2):387–396
56. Mukhopadhyay Swati, Layek GC, Samad SA (2005) Study of MHD boundary layer flow over a heated stretching sheet with variable viscosity. Int J Heat Mass Transf 48:4460–4466
57. Mukhopadhyay S, Layek GC (2012) Effects of variable fluid viscosity on flow past a heated stretching sheet embedded in a porous medium in presence of heat source/sink. Meccanica 47(4):863–876
58. Islam N, Islam B, Mazumdar HP, Lahiri J (2011) Application of the Lie groups of transformations for an approximate solution of MHD flow of a visco-elastic second grade fluid. Appl Sci 13:65–73
59. Shah NA, Animasaun IL, Ibraheem RO, Babatunde HA, Sandeep N, Pop I (2018) Scrutinization of the effects of Grashof number on the flow of different fluids driven by convection over various surfaces. J Mol Liq 249:980–990
60. Animasaun IL, Ibraheem RO, Mahanthesh B, Babatunde HA (2019) A meta-analysis on the effects of haphazard motion of tiny/nano-sized particles on the dynamics and other physical properties of some fluids. Chin J Phys 60:676–687
61. Wakif A, Animasaun IL, Narayana PS, Sarojamma G (2020) Meta-analysis on thermo-migration of tiny/nano-sized particles in the motion of various fluids. Chin J Phys 68:293–307
62. Siddiqui AM, Shoaib M, Rana MA (2017) Three-dimensional flow of Jeffrey fluid along an infinite plane wall with periodic suction. Meccanica 52(11):2705–2714
63. Siddiqa S, Begum N, Hossain MA, Shoaib M, Reddy Gorla RS (2018) Radiative heat transfer analysis of non-Newtonian dusty Casson fluid flow along a complex wavy surface. Numer Heat Transf Part A Appl 73(4):209–221
64. Awais M, Raja MAZ, Awan SE, Shoaib M, Ali HM (2021) Heat and mass transfer phenomenon for the dynamics of Casson fluid through porous medium over shrinking wall subject to Lorentz force and heat source/sink. Alex Eng J 60(1):1355–1363
65. Ahmad I, Cheema TN, Raja MAZ, Awan SE, Alias NB, Iqbal S, Shoaib M (2021) A novel application of Lobatto IIIA solver for numerical treatment of mixed convection nanofluidic model. Sci Rep 11(1):1–16

Publisher's Note Springer Nature remains neutral with regard to jurisdictional claims in published maps and institutional affiliations.